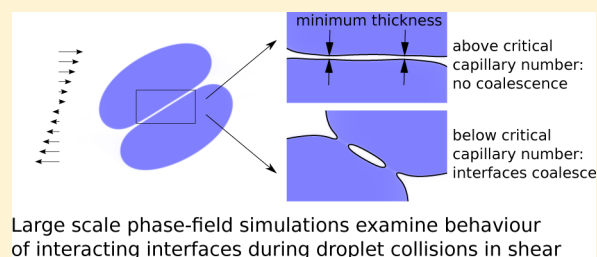


The Critical Conditions for Coalescence in Phase Field Simulations of Colliding Droplets in Shear

Orest Shardt,^{*,†} Sushanta K. Mitra,[‡] and J. J. Derksen[†]

[†]Department of Chemical and Materials Engineering and [‡]Department of Mechanical Engineering, University of Alberta, Edmonton, AB T6G 2R3, Canada

ABSTRACT: Simulations have been performed using the free-energy binary-liquid lattice Boltzmann method with sufficient resolution that the critical capillary number for coalescence was determined for collisions between droplets in simple shear with a small initial offset in the shear gradient direction. The simulations were used to study the behavior of the interacting interfaces and the film between them during collisions over a wide range of capillary numbers with emphasis on near-critical conditions. From these three-dimensional simulations with deforming interfaces, several features of the evolution of the film between the drops were observed. The critical film thickness was determined to be similar to the interface thickness, a power law described the dependence of the minimum film thickness on the capillary number in collisions without coalescence, and an inflection point was found in the dynamics of the minimum distance between drops that eventually coalesce. The rotation of the film and the flow in it were also studied, and a reversal in the flow was found to occur before coalescence. The mobility of the phase field was therefore important in the continued thinning of the film at the points of minimum thickness after the flow reversal. A comparison of the critical capillary number and critical film thickness in the simulations with the values for experiments in confined simple shear indicated that the effective physical radius of the simulated droplets was on the order of several micrometers. The results are significant for simulations of droplet interactions and emulsion flows in complex geometries and turbulence because they demonstrate the necessary scale of the computations and how parameters, such as the interface thickness and phase field mobility, should be selected for accurate results.



INTRODUCTION

Phase field models for computing multiphase flows describe interface motion and deformation in a way that conveniently handles the topological changes of breakup and coalescence. These methods have been used to study the deformation and breakup of droplets in simple shear^{1,2} and microfluidic junctions³ as well as the motion of three phase contact lines.^{4–7} In fact, simulations of contact line motion with the Cahn–Hilliard⁸ model have matched molecular dynamics simulations.^{5,9} While these interfacial flow phenomena have been studied in detail with phase field methods, the interactions between interfaces that lead to coalescence have received comparatively little attention. A key reason is the need for high resolution: the colliding droplets in simulations of coalescence must be significantly larger than the films that can form between them. The difficulty of achieving sufficient resolution led to the observation that coalescence was too easy in simulations,¹⁰ and methods with suppressed coalescence were developed.^{11,12} While models with suppressed coalescence are useful for studying flows where coalescence does not occur, they cannot be used to study the transition to coalescence. The ability to perform simulations with accurate predictions of the conditions for coalescence would be useful in a wide variety of applications. Examples include droplet collisions in shear, confined droplet flows in microchannels,¹³ and situations where breakup and coalescence must both be modeled correctly, such

as the droplet size distributions of falling raindrops¹⁴ and emulsions in turbulence.^{15,16} Consequently, there is a need to understand the conditions for and dynamics of coalescence in phase field simulations of fluid mixtures to assess their ability to describe coalescence phenomena. Due to its physical foundations and success in describing other flow phenomena, the Cahn–Hilliard model is the focus of this work. We perform simulations of droplet collisions in confined simple shear flow, a flow configuration in which the critical conditions for coalescence have been studied experimentally.^{17,18}

Simulations of colliding droplets in shear were first performed by Loewenberg and Hinch¹⁹ using a boundary integral method and preceded the experimental work of Guido and Simeone,²⁰ who found agreement with the simulations. These experiments did not provide the critical conditions for coalescence, but revealed the trajectories and deformation of drops during collisions at different conditions. A sample experimental trajectory was reproduced in simulations by Cristini et al.²¹ Earlier experiments by Bartok and Mason²² and Allan and Mason²³ showed that deformation of the drops was needed for their separation in the velocity gradient direction to increase during a collision. The critical conditions for

Received: August 21, 2014

Revised: November 13, 2014

Published: November 14, 2014

coalescence in primarily extensional linear shear flows were studied by Yang et al.,²⁴ and the effect of the viscosity ratio was determined.²⁵ Mousa et al.²⁶ studied the coalescence efficiency of droplets in simple shear flow, and recently the critical conditions for coalescence in confined simple shear flow were determined.^{17,18} In these and previous experimental studies, flow inertia has been negligible. Simulations with a front-tracking finite difference method have examined the effects of finite inertia, confinement, and viscosity ratio.^{27–29}

While the purpose of these previous studies was to examine the self-diffusion of sheared droplets due to collisions, the focus of our work is not on the trajectories and deformation of colliding droplets but rather on determining the critical conditions for coalescence in phase field models and studying the behavior of the film between the drops at near-critical conditions. In simulations with the free-energy lattice Boltzmann method,⁶ we have previously found³⁰ conditions at which colliding droplets in impulsively started simple shear flow do not coalesce. In these simulations, the interface profile was resolved well to ensure that coalescence occurred as a consequence of the phase field dynamics without artifacts of a poorly resolved diffuse interface. The resolution of these previous simulations proved insufficient to determine the effective physical size of the simulated droplets, and we now address this question by presenting simulations with twice the previous droplet size. Due to the larger drop size, we can now determine the critical capillary number for coalescence at an initial offset in the velocity gradient direction of 20% the diameters of the drops, near the value (16%) in the experiments of Chen et al.¹⁷

In the sections that follow, we briefly describe the numerical method and sample results with twice the resolution of our previous work.³⁰ We then present the details of the interface behavior during a collision, including the evolution of the minimum distance between the droplets and the orientation of the film between them. We compare the critical capillary number in the simulations with experimental values, accounting for differences in the conditions, and examine the role of diffusion in the behavior of the thin film between the drops. We conclude with remarks on the prospects of predictive simulations of coalescence with Cahn–Hilliard-type phase field models.

NUMERICAL MODEL

The numerical method and its implementation are the same as we have used previously;³⁰ the scale of the computations is, however, significantly larger. We use the free-energy binary-liquid lattice Boltzmann method⁶ to perform the simulations. In general, lattice Boltzmann methods (LBMs) compute flows by evolving a discrete probability density function for the velocity distribution of fictitious fluid molecules.³¹ This is typically implemented in a two-step process: motion (or streaming) of the molecules along the discrete directions connecting adjacent lattice nodes and collisions between molecules, which are modeled as relaxation toward an equilibrium velocity distribution. We use the BGK (Bhatnagar–Gross–Krook³²) collision operator. The bulk flow properties (density, velocity, and stress) are computed by summation of moments of the probability distribution, and provided that flow speeds are slow (compared to the speed of sound in the lattice), they satisfy the incompressible Navier–Stokes equation.

To model a mixture of two liquids, a second probability density function is used to compute the advection and diffusion of a scalar composition variable, the phase field ϕ . The simulations are three-dimensional, and both the hydrodynamic and phase field lattices have

19 discrete velocities. The phase field evolves according to the advection–diffusion equation.

$$\frac{\partial \phi}{\partial t} + \nabla \cdot (\phi \vec{u}) = M \nabla^2 \mu \quad (1)$$

where $\mu = A\phi(\phi^2 - 1) - \kappa \nabla^2 \phi$ is the chemical potential and M is the mobility. The phase field dynamics and flow are coupled through a modified pressure tensor in the flow solver. With the specified chemical potential, the fluid separates into two phases with $\phi = \pm 1$. The two parameters A and κ in the chemical potential together specify the thickness and tension of the interface, respectively. The steady solution for ϕ across a planar interface between two semi-infinite domains is

$$\phi(x) = \tanh(\zeta^{-1}x) \quad (2)$$

where $\zeta = (2\kappa/A)^{1/2}$ is a characteristic length of the distance over which ϕ varies between its values in the two domains (± 1). Based on previous work,³⁰ all simulations were performed with $\zeta = 2$ (lattice spacings) to ensure that the interface is well-resolved. It was previously shown³⁰ that simultaneously doubling ζ , the droplet radius, and the domain size does not change the behavior of colliding drops. Therefore, with $\zeta = 2$, coalescence is a consequence of the dynamics of the phase field without significant discretization errors. The thickness of the interface is larger than the characteristic length ζ : 95% of the change in composition across an interface occurs over the distance 3.7ζ ; 99% of the change occurs over 5.3ζ . For large droplets (with a radius that exceeds 20 lattice nodes¹⁰), the interfacial tension σ may be determined from the excess free energy of a planar interface (eq 2) to be.

$$\sigma = \frac{2\sqrt{2}}{3} \sqrt{\kappa A} \quad (3)$$

The conditions of the simulations can be described with several dimensionless numbers that capture the hydrodynamics, interfacial properties, and geometry of the simulated system. Figure 1 shows a

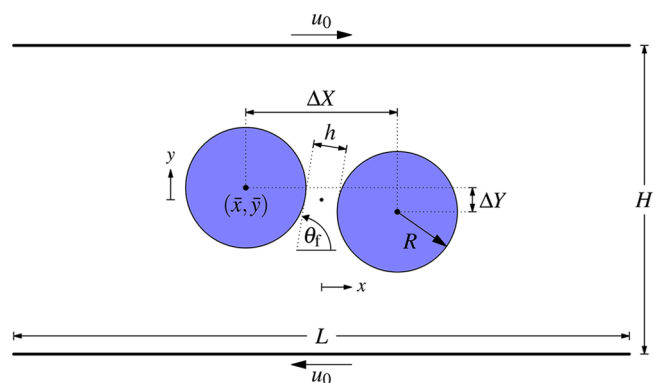


Figure 1. Schematic of the cross section through the simulated three-dimensional domain including the definitions of variables that describe the geometry and conditions of the colliding droplets. The omitted z axis points out of the page, and this cross section is at $z = 0$.

schematic of the cross section through the center of the simulation domain along the omitted z axis. This figure provides the definitions of the variables that describe the initial geometry of the simulated system and the variables of interest for the later analysis. Two shear planes separated by a distance H move in opposite directions at a speed u_0 . Between them, two droplets with equal radii R are located in the middle of the domain, separated by a (nondimensional) horizontal separation $\Delta X/(2R) = 1.26$ and a vertical offset $\Delta Y/(2R) = 0.2$. The confinement of the droplets is $2R/H = 0.39$. The minimum distance between the interfaces of the droplets is h , and the film inclination angle θ_f is the angle of the tangent to the interface of the higher droplet at the point of minimum distance from the lower droplet. The other dimensions of the system are a length $L = 2H$ in the x direction

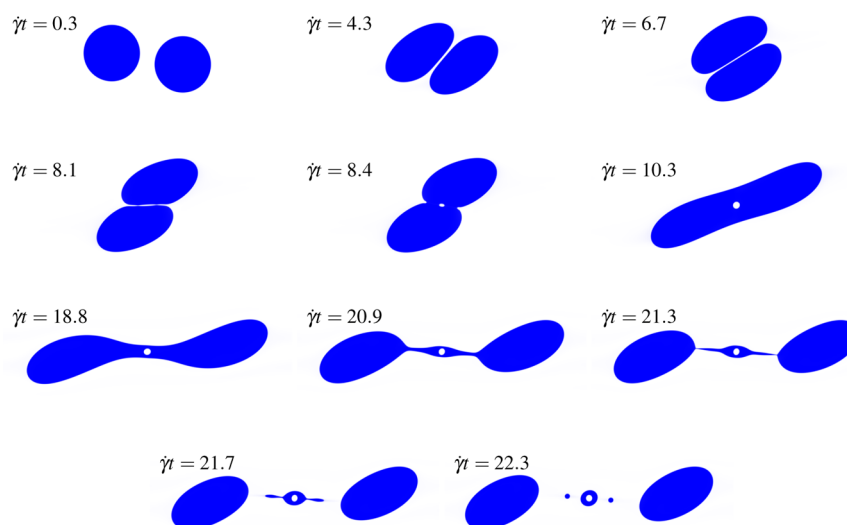


Figure 2. Coalescence and subsequent breakup at $Ca = 0.200$, $Re = 1$, $\Delta X/(2R) = 1.26$, $\Delta Y/(2R) = 0.2$, and $2R/H = 0.39$.

(shear direction), a height H in the y direction (velocity gradient direction), and a width $W = H$ in the z direction (vorticity direction). The simulations only compute one-quarter of the full $L \times H \times W$ system because symmetry boundary conditions are employed along the $z = 0$ and $z = W/2$ planes and a rotational symmetry condition is used at $y = 0$. The $x = \pm L/2$ boundaries are periodic. While the hydrodynamic field has a shear condition at $y = H/2$, the phase field has a symmetry condition on this plane. The shear condition is implemented using the method of Ladd³³ because this method conserves the density of the fluid along the boundary, which is an important feature for our simulations that run for several million time steps.

The Reynolds number of the shear flow is

$$Re = \frac{\dot{\gamma}R^2}{\nu} \quad (4)$$

based on $\dot{\gamma}R$ as the characteristic speed, where $\dot{\gamma} = 2u_0/H$ is the shear rate, and the radius R of both droplets as the characteristic length. The kinematic viscosity of the droplet and bulk fluids is $\nu = 1/6$ (in lattice units which corresponds to a relaxation time of one for the collision operator of the LBM hydrodynamic density distribution). All simulations are performed with $Re = 1$ as in previous work.³⁰ This choice of Re is sufficiently high that the explicit numerical method remains efficient yet low so that inertial effects do not dominate, allowing comparison with previous experimental work.¹⁷

We define the capillary number Ca as

$$Ca = \frac{\rho\nu\dot{\gamma}R}{\sigma} \quad (5)$$

where $\rho = 1$ (in lattice units) is the density of the fluid. The interface Péclet number

$$Pe = \frac{\dot{\gamma}R\zeta}{MA} \quad (6)$$

expresses the ratio of the rates of advection and diffusion of ϕ over the characteristic distance of the interface thickness. As in previous work,³⁰ we use $Pe = 10$, a value at which simulations of droplet deformation in shear were found to be accurate.³ In the specification of the mobility in the LBM for the phase field, the relaxation time in the collision operator is kept fixed at one.

We present simulations in which the radius of each droplet spans 200 lattice spacings, twice the radius of our previous work³⁰ and 100 times the characteristic length ζ of the diffuse interface. The simulated domain is 8 times larger than previously, spanning $2048 \times 512 \times 512$ lattice nodes (which is one-quarter of the full system domain due to symmetry). We consider the range of capillary numbers from 0.01 to

0.25 with more simulations performed near the critical capillary number for coalescence, approximately 0.2.

Implementation. The numerical model is highly amenable to parallelization because the computations at each lattice node of the domain require information from only the adjacent nodes. The locality of the calculations also allows acceleration of the simulations through the use of graphics processing units (GPUs) instead of conventional (multicore) central processing units (CPUs). The limited memory available on GPU devices, however, necessitates splitting the computational domain across multiple devices and communicating boundary layers between them. The simulations were run on two Compute/Calcul Canada GPU clusters with NVIDIA Tesla M2070 GPUs. One cluster has three GPUs per node (of which 66 GPUs were used); the other, which has two per node (of which 64 were used), performs the computations slightly faster. The average speed on the faster system is 1248 million lattice updates per second (Mlups). In comparison, an implementation of the same method runs at 2 Mlups on eight conventional CPU cores.² On both systems, communication between GPUs on the same node occurs over a system bus, while communication over the Infiniband interconnect between nodes is performed with a Message Passing Interface (MPI) library. A cross section of the phase and velocity fields through the middle of the domain is saved every 32 000 time steps (a nondimensional time interval of $\dot{\gamma}\Delta t = 0.133$). All computations are performed with double precision and with error checking and correction (ECC) enabled on the GPUs.

RESULTS AND DISCUSSION

Since the critical capillary numbers at the conditions of the new simulations, specifically $R/\zeta = 100$ and $\Delta Y/(2R) = 0.2$, were not known, several capillary numbers between 0.01 and 0.25 were chosen to explore the parameter range and observe the nature of the collisions. These simulations also provided the intervals that were then bisected repeatedly to determine the critical capillary numbers. At the conditions of the present and previous work,³⁰ two critical capillary numbers separate three possible outcomes. Below the lower critical capillary number, droplets coalesce. Above the upper critical capillary number, the droplets slide over each other and their interfaces never merge. Between the two critical values, the droplet interfaces merge, the bridge between them grows, and eventually this bridge breaks because the merging droplet is sheared apart faster than the bridge grows.³⁰ A sample simulation at $Ca = 0.200$, which is in this intermediate region and near the upper critical capillary number, is shown in Figure 2. The visualizations of cross

sections through the droplets reveal several fine details due to the high resolution of the simulations. After the droplets approach, a thin film forms with an initial inclination angle $\theta_f \approx 45^\circ$. The shapes of the droplets until this time qualitatively match the front-tracking simulations of Olapade et al.²⁷ at similar conditions ($Re = 2$, $Ca = 0.2$, $\Delta X/(2R) = 1.25$, and $\Delta Y/(2R) = 0.125$). They are also similar to boundary integral simulations at $Ca = 0.3$ with $\Delta X/(2R) = 5$ and $\Delta Y/(2R) = 0.25$.¹⁹ While Olapade et al.²⁷ and Loewenberg and Hinch¹⁹ do not simulate coalescence, in our simulations, the droplets start to slide over each other, and the film rotates and thins until two dimples form when the film is parallel to the shear direction. As the interfaces merge, a drop of the bulk fluid is trapped in the growing bridge. As this bridge grows, the lobes at the ends continue to be sheared apart, and the bridge thins and rotates. The end lobes eventually pinch off. The bridge retracts, leaving an encapsulated droplet of the bulk fluid in the center and a droplet between this central droplet and each of the recently pinched-off drops. At $Ca = 0.202$, the breakup of the bridge produces two additional drops (Figure 3). The number of

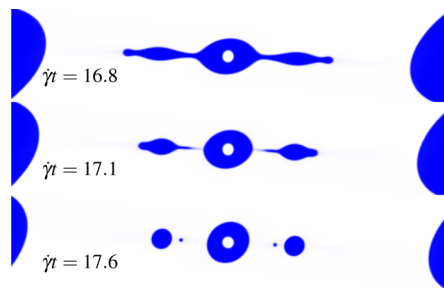


Figure 3. Breakup of the temporarily coalesced drop at $Ca = 0.202$. Compared to $Ca = 0.200$ (Figure 2), the drop breaks earlier and two more drops form. The full domain has been cropped to focus on the breaking bridge.

drops and their positions and sizes are notably similar to the experiments and simulations of filament breakup by Tjahjadi et al.³⁴ for equal drop and external liquid viscosities. These sample simulations shown in Figures 2 and 3 are very close to the upper critical capillary number. This upper critical Ca is between 0.2020 and 0.2028 based on a sequence of simulations that successively bisected the initial range 0.2–0.25. A precise estimate of the lower critical capillary number that determines whether the growing bridge breaks is not available from the simulations of this study. The lower critical capillary number is between 0.1 and 0.2, and likely between 0.15 and 0.2, but the simulation at 0.15 was stopped immediately after the interfaces merged to provide computing resources instead for simulations near the upper critical Ca . Complete coalescence at $Ca = 0.15$ is expected because $\theta_f > 0$ at the time of coalescence. In this orientation, the applied shear compresses the growing bridge rather than stretching it. In all the cases where the droplet breaks after coalescing, the capillary number is less than that required to break an initially stationary drop. Breakup after temporary coalescence occurs because the bridge does not grow quickly enough to achieve a near-equilibrium shape before the growing drop is sheared apart³⁰ and not because the critical Ca for breakup in an impulsively started flow is exceeded by the coalesced drop. With $Re = 1$ and equal droplet and external viscosities, initially spherical droplets in an impulsively started shear flow break when the capillary number exceeds 0.28.^{2,35} Since the coalesced drop has twice the volume of each initial

drop, its radius and capillary number would be $2^{1/3} \approx 1.26$ times larger than those of the initial drops. Therefore, the droplet formed after coalescence must break when the capillary number of the two initial droplets exceeds 0.22, which is higher than the critical capillary number for coalescence at the simulated conditions.

Sample trajectories of the upper droplet at capillary numbers between 0.01 and 0.25 are shown in Figure 4. The droplets

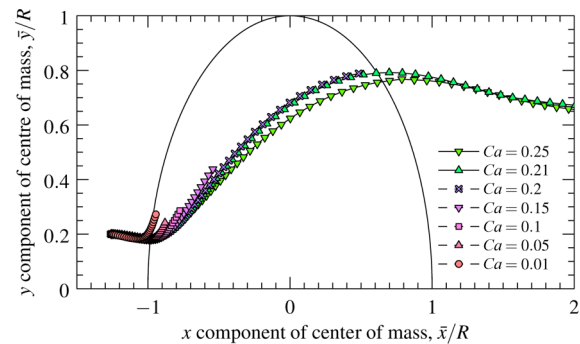


Figure 4. Position of the center of mass (\bar{x}, \bar{y}) of the upper droplet during collisions at several capillary numbers. The solid line shows the trajectory of one sphere in a pair of touching rigid spheres rotating about the origin. The time interval between consecutive symbols is $\dot{\gamma}\Delta t = 0.133$.

coalesce at progressively later stages of the collision with increasing capillary number. These trajectories reveal two features of the collisions. The first feature is the compression and deformation of the droplets. For reference, the solid line in Figure 4 shows the circle that would be traced out by a sphere rotating in contact with another identical sphere with the same size as the initially spherical droplets. The centers of mass of the two colliding droplets approach much closer than the initial diameters of the drops. At $Ca = 0.25$, the minimum distance between the centers of mass of the two drops is 58% of the diameters. Only at the lowest capillary number considered ($Ca = 0.01$) does the trajectory temporarily follow the path of rigidly rotating spheres before coalescing. We point out that, at this low capillary number, the droplets coalesce slightly later and higher than at $Ca = 0.05$. The second noteworthy feature of the trajectories is the absence of an abrupt change as the capillary number crosses the upper critical value. As the critical capillary number is approached from above and below, the trajectories converge to the same shape. The motion of the droplets is unaffected by the details of the behavior of the film between them unless this film ruptures and triggers a change in the topology of the fluid domain. As will be shown later, the film behavior changes significantly in several ways as the capillary number approaches the upper critical value.

We briefly compare the trajectory of a noncoalescing drop ($Ca = 0.21$ in Figure 4) with other simulations reported in the literature for similar conditions. The vertical position of this trajectory achieves a minimum soon after the shear flow starts and later reaches a maximum of $\bar{y}/R = 0.79$. Guido and Simeone²⁰ obtained a peak of $\bar{y}/R = 0.88$, independent of the initial vertical offset in experiments at low Re , $Ca = 0.13$, and a droplet viscosity 0.36 times the external viscosity. Simulations by Loewenberg and Hinch¹⁹ with equal viscosities, $\Delta Y/(2R) = 0.25$, and $Ca = 0.1$ and 0.3 show peaks at $\bar{y}/R = 0.88$ and 0.77 , respectively. Front tracking simulations have been used to study collision trajectories under a wide range of conditions, including

finite inertia.^{27–29} A maximum \bar{y} is not seen in simulations of unconfined droplets at $Re = 1$, equal viscosities, and $Ca = 0.2$,²⁷ but a finite domain size causes a maximum to appear.²⁷ The presence of an initial downward trajectory has been observed by others. It is enhanced by high Re , high Ca , small vertical offset, large horizontal separation, and low drop viscosity relative to the external fluid.^{27,28} The purpose of these previous studies was, in general, to determine the increase in vertical offset between droplets after a collision and study the self-diffusion of drops in emulsions. Our interest, however, is in the details of the film behavior and we do not consider the trajectories in further detail.

In the sections that follow, we examine the behavior of the film between the drops at capillary numbers near the upper critical value. Of the two critical capillary numbers, the upper critical number decreases faster with increasing radius of the drops (relative to the interface thickness).³⁰ For sufficiently large drops, only one critical Ca separates the conditions for coalescence and sliding; temporary coalescence is not observed. These trends were determined for collisions with higher vertical offsets (0.86 and 0.6) than the present work, and we assume that the same trends hold for $\Delta Y/(2R) = 0.2$, specifically that the lower critical Ca decreases slower than the upper critical Ca as R/ζ increases. Therefore, it is the upper critical Ca that should be compared with critical Ca for coalescence of larger droplets, for which experimental critical capillary numbers are available but simulations are not feasible due to excessive computational demands. In the remainder of this paper, the upper critical capillary number is denoted \bar{Ca}_c and we do not discuss the lower critical Ca further.

Film Behavior. Due to the large domain size and limited computing and storage resources (20 GiB is required to store all values of ϕ , ρ , and the three velocity components in the $2048 \times 512 \times 512$ domain), we analyze cross sections through the middle of the domain ($z = 0$) in the $x - y$ plane. The interface is located where $\phi = 0$, and we calculate the minimum distance between polygonal droplet contours determined by bilinear interpolation of the values of ϕ at each lattice node.³⁶ We focus on capillary numbers near the critical value and examine the minimum distance between the two interface contours when they are in close proximity and a film can be considered to exist. Figure 5 shows the evolution of the minimum distance between the drops as a function of time for all simulations. Three stages are evident in the interaction between the droplets for capillary numbers in the interval $0.20 \leq Ca \leq 0.25$: an approach phase that lasts until $\gamma t \approx 5$, a film

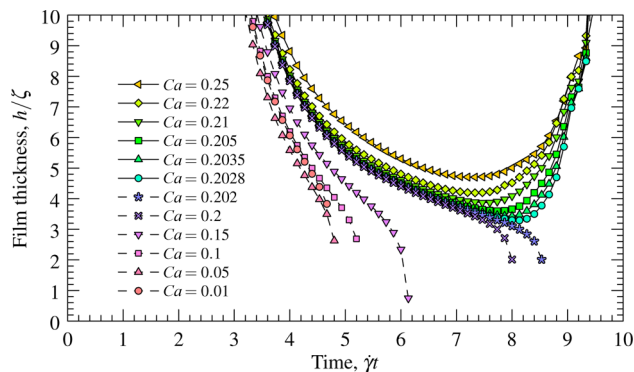


Figure 5. Minimum distance between droplets as a function of time for collisions at capillary numbers between 0.01 and 0.25.

thinning stage until $\gamma t \approx 8.5$ at the latest, and finally a separation or coalescence stage. At lower capillary numbers, that is, $Ca < 0.2$, droplets coalesce before a distinct film thinning stage occurs.

Among the simulations in which the interfaces never merge, the smallest film thickness observed is 3.3ζ with $Ca = 0.2028$. Over this distance, 93% of the change in ϕ across a flat interface (eq 2) occurs. The minimum film thickness is therefore similar to the thickness of the interface, and only a small overlap of adjacent interfaces is needed to start coalescence. While the range for the critical capillary number (0.202–0.2028) is at most 0.4% of its value, the minimum film thickness at the lowest supercritical capillary number (0.2028) provides a significantly less precise estimate of the critical thickness. The dependence of the minimum film thickness on the capillary number reveals a better estimate of the critical thickness. A power law model $h_{\min} - h_c = \alpha(Ca - \bar{Ca}_c)^n$ describes the dependence well. In this model, the difference between the minimum film thickness h_{\min} and the critical film thickness h_c is proportional to a power of the difference between the capillary number and the critical capillary number \bar{Ca}_c . The capillary number Ca is an input to the simulations, h_{\min} is an output, and h_c , α , \bar{Ca}_c , and n are fitting parameters. As shown in Fig. 6, the fit is excellent, though we note that four

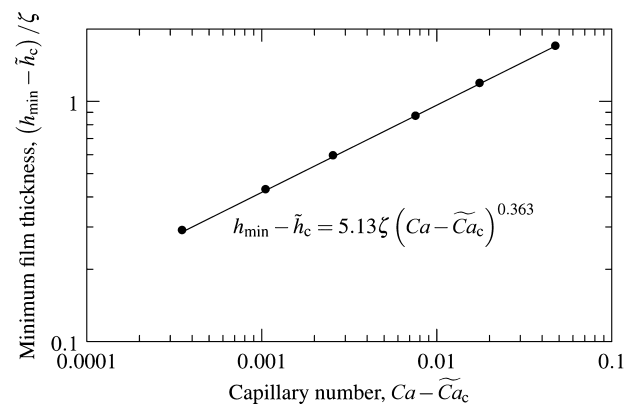


Figure 6. Dependence of the minimum film thickness on the capillary number. The proportionality factor, exponent, critical film thickness ($\bar{h}_c/\zeta = 3.00$), and critical capillary number ($\bar{Ca}_c = 0.20245$) were determined by least-squares fitting.

model parameters have been estimated from six simulations. A least-squares fit provided the estimated critical capillary number $\bar{Ca}_c = 0.20245$ and the estimated critical film thickness $\bar{h}_c/\zeta = 3.00$. The fitted exponent is $\bar{n} = 0.363$, and the proportionality factor is $\bar{\alpha} = 5.13$. The fitted critical capillary number is higher than the highest subcritical Ca that has been simulated (0.202), raising confidence in the model. The critical film thickness cannot be determined more precisely with the current resolution of the simulations. Based on the fitted model, the capillary number may only exceed the critical value by $3 \times 10^{-4}\%$ for the minimum film thickness to be within 1% of the critical value. At the lowest supercritical Ca we simulate (0.2028), the minimum film thickness is 0.29ζ , or 0.58 lattice nodes, higher than the critical value, which is 10% of the critical thickness. To determine a more precise critical thickness, simulations with a thicker interface, i.e. $\zeta > 2$ and a proportionally larger droplet radius and domain, are needed. Further bisections of the critical range with $\zeta = 2$ are not worthwhile due to the imprecision of minimum film thicknesses

obtained from interface contours that are computed by interpolating between the values of ϕ at lattice nodes.

The dynamics of the film thinning process can be understood better by considering how the rate of film growth/thinning varies with the film thickness near the critical conditions. Figure 7 shows a phase portrait of the film thinning dynamics at near-

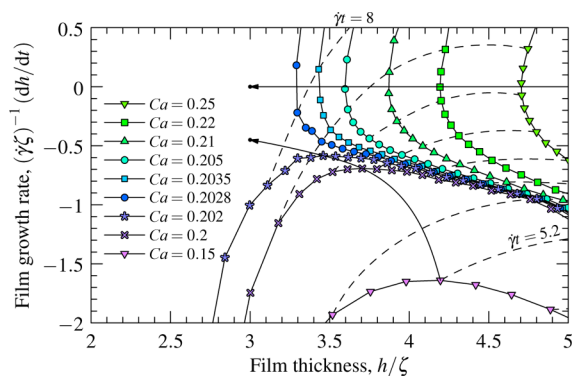


Figure 7. Dynamics of the film thickness h at near-critical capillary numbers. The dashed curves connect points at equal times spaced by $\dot{\gamma}\Delta t = 0.4$ with the latest (upper left) at $\dot{\gamma}t = 8$. Arrows indicate the locations of the estimated critical minimum thickness and potential position of the critical minimum thinning rate.

critical capillary numbers. Time proceeds from the bottom right to the top right (supercritical Ca) or the bottom left (subcritical Ca). States in the upper left quadrant of the figure, where the film would grow while having a subcritical thickness, are not reached. The phase portrait emphasizes the sensitivity of the collision outcome and film dynamics to small changes in the capillary number, and it reveals several interesting features of the film drainage process. At supercritical capillary numbers, a minimum film thickness must necessarily exist, and the thinning rate must be zero when the film is thinnest. An arrow along $dh/dt = 0$ indicates the extrapolated critical film thickness (Figure 6). As $Ca \downarrow Ca_c$, dh/dt increases quickly soon after $dh/dt = 0$ (see also Figure 5). This can be seen as a vertical straightening of the trajectory in phase space as it crosses dh/dt with decreasing Ca and a corner in the film thickness as a function of time (at $\dot{\gamma}t \approx 8.5$ in Figure 5). These results suggest that dh/dt soon after the time of minimum thickness may diverge as $Ca \downarrow Ca_c$.

The bisection method for finding the critical conditions led to few simulations at subcritical capillary numbers. Figure 7 shows that the presence of a minimum thinning rate is a unique feature of the subcritical simulations, a feature that can also be seen as an inflection point in Figure 5. In general, the film thins at a decreasing rate until reaching either a minimum thickness (and then separating) or a minimum thinning rate (and then accelerating to coalescence). The minimum thinning rate decreases as the capillary number increases to its critical value, but the two highest subcritical cases do not clearly indicate whether the critical minimum thinning rate reaches zero or a particular positive value (negative dh/dt). The region of inadmissible states in Figure 7 is therefore not yet precisely known. The film thickness at the time when the thinning rate reaches its minimum exceeds the critical film thickness, and it decreases as $Ca \uparrow Ca_c$. Therefore, the outcome of subcritical simulations is known the moment a minimum thinning rate occurs, which is before the critical thickness is reached. Furthermore, at near-critical Ca , the film rotates rapidly, and

therefore, its inclination at the time of coalescence differs from the inclinations when the thinning rate is minimum and when the thickness crosses the critical value. This raises questions about whether the attainment of a critical film thickness is an appropriate phenomenological model for determining when coalescence occurs. This criterion has been used to specify when meshes of nearby droplets are connected in some simulation methods.^{37,38}

Figures 5 and 7 have shown the outcome of the competition between the hydrodynamic forces that pull the droplets apart in the late stages of the collision and the film flow and phase field dynamics that lead to coalescence. It is important to emphasize that the dynamics described in these figures are for the distance between the two closest points on the droplets, and the behavior in the whole film is more complex. An examination of the flow in a cross-section of the film at the lowest supercritical capillary number (0.2028) reveals an interesting feature of the flow in the film near the critical conditions. The flow field \vec{u} in the film may be considered the sum of a rigid rotation at the rate with which the film is rotating ($d\theta_f/dt$) and a velocity relative to this rigid rotation. Figure 8 shows that this relative

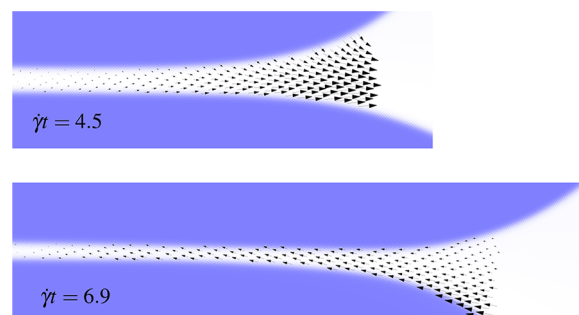


Figure 8. Flow fields in the film relative to rigid rotation at the rotation rate of the film $d\theta_f/dt$ for the simulation with $Ca = 0.2028$ at times $\dot{\gamma}t = 4.5$ (top) and 6.9 (bottom). The images have been rotated so that the film is horizontal. One arrow is shown for every fourth lattice node in both directions. To illustrate the structure of the flow, the lengths of the arrows are scaled relative to the maximum relative flow speeds at each time, which are $0.18\dot{\gamma}R$ ($\dot{\gamma}t = 4.5$) and $0.12\dot{\gamma}R$ ($\dot{\gamma}t = 6.9$).

fluid motion is out of the film at $\dot{\gamma}t = 4.5$, as expected for a draining film. However, by $\dot{\gamma}t = 6.9$, the flow reverses, and now points into the film. These relative flow speeds are small, about one tenth of the characteristic speed $\dot{\gamma}R$, and should be compared with spurious currents (in the absence of applied shear) to ensure that the relative flows are not a similar magnitude. Though a stationary simulation was not performed with $R = 200$, results for $R = 50$ and 100 indicate that spurious currents are sufficiently low. When Re and Ca are kept constant as R is increased by a factor of two, $\dot{\gamma}R$ and σ are halved. With increasing R , spurious currents decrease because of the larger radius of curvature of the interface and the lower interfacial tension. The decrease in the maximum spurious speed appears to match the decrease in $\dot{\gamma}R$: maximum spurious speeds are $0.008\dot{\gamma}R$ with $R = 50$ and $0.009\dot{\gamma}R$ with $R = 100$, both at $Ca = 0.1$. For $R = 200$ and $Ca = 0.1$, spurious speeds are not expected to exceed $0.01\dot{\gamma}R$ and are likely lower for $Ca = 0.2$ due to the lower interfacial tension. The relative flow in the film is therefore an order of magnitude faster than the expected maximum spurious currents around a stationary droplet with the same interfacial tension.

The presence of a reversal in the film flow can also be seen in the absolute (not relative to rotation) flow field. Over the same time interval that the relative flow in the film reverses, the vorticity $\omega = \partial u_y / \partial x - \partial u_x / \partial y$ (calculated by central finite differences of the velocity data) in the film changes sign from positive (counterclockwise) at $\dot{\gamma}t = 4.5$ to negative (clockwise) at $\dot{\gamma}t = 6.9$, as illustrated in Figure 9. The flow fields do not

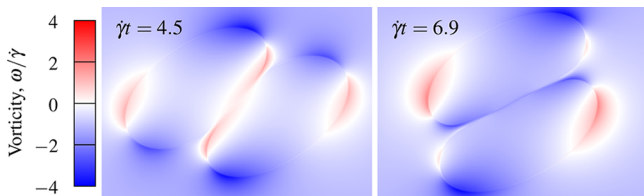


Figure 9. Vorticity $\omega = \partial_x u_y - \partial_y u_x$ (normalized by the applied shear rate $\dot{\gamma}$) in the film, the drops, and the nearby fluid at $\dot{\gamma}t = 4.5$ (left) and 6.9 (right) for the collision with $Ca = 0.2028$.

change significantly near the critical capillary number and the same reversal phenomena were found in both sub- and supercritical simulations near Ca_c . The reversal therefore happens before coalescence when the capillary number is sufficiently high: at $Ca = 0.202$, coalescence does not occur until $\dot{\gamma}t = 8.5$. The reversal of the flow in the film occurs surprisingly early in the interaction: the film orientation angle is positive, and the centers of mass of the droplets are not yet vertically aligned (they align at $\dot{\gamma}t \approx 7.1$). The reversal therefore occurs during what is usually considered the “compressive” stage of the collision.

When the flow reversal occurs, the thickness of the film is between one and two times the interface thickness. One should therefore consider whether the flow in the film is adequately resolved with this thickness. Simulations of confined droplet motion in a channel with the same free-energy binary-liquid LBM have been reported.³⁹ The thickness of the film between the drop and the wall was found to be accurate when it was at least twice the interface thickness. However, the thickness of the film changed only 4% when the resolution was halved. We therefore consider that the flow in the film is reasonably resolved until the thickness of the film approaches the critical thickness (which is similar to the interface thickness). It is important to note that one cannot have full resolution of the film (by choosing R/ζ so that for example $h_{\min} \gtrsim 8\zeta$ to meet the criterion given by Kuzmin et al.³⁹) yet still observe coalescence, which requires the film thickness to reach the critical film thickness $h_c = 3\zeta$. Low resolution of the flow in the film is not the reason for coalescence: coalescence occurs due to the phase field dynamics and gradients in chemical potential in the adjacent interfaces.

The continued decrease of the minimum distance between the interfaces despite the reversal of the flow in the film occurs due to fluxes of ϕ that counteract sharp gradients of chemical potential. Based on the film thickness and time when the reversal occurs, we may consider the mobility of the phase field to contribute significantly to the dynamics of h in the portion of Fig. 5 where $h \lesssim 5\zeta$. Consequently, diffusion of ϕ contributes to the dynamics of h throughout the ranges of time, thickness, and growth rate shown in the phase portrait, Figure 7. This choice is consistent with a convergence study of the film thickness at supercritical capillary numbers (see Appendix: Convergence of Film Thickness) in which the film thicknesses for two different Pe cross when $h = 6\zeta$ at near critical Ca . The

independence of the film thickness to the Péclet number prior to the crossover thickness suggests that the mobility does not have a significant effect on interfaces that are further apart.

We look more closely now at the rotation and thinning of the film during near-critical collisions. Figure 10 shows the film

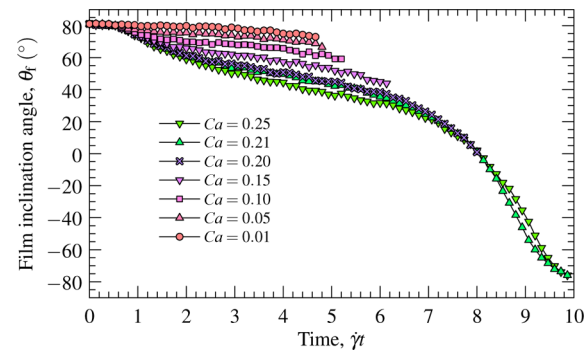


Figure 10. Film inclination angle as a function of time for several capillary numbers.

inclination angle as a function of time for several capillary numbers. Like the center of mass (Figure 4), the sub- and supercritical inclination angles converge as $Ca \rightarrow Ca_c$. Figure 11

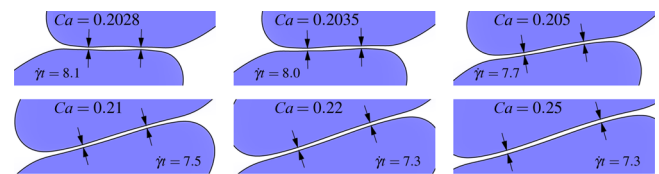


Figure 11. Cross sections through the droplets at the time of minimum film thickness for $Ca = 0.2028, 0.2035, 0.205, 0.21, 0.22,$ and 0.25 . Arrows indicate the locations where the films are thinnest.

illustrates the shapes of the thinnest films at the simulated capillary numbers, and Figure 12 shows the films when the

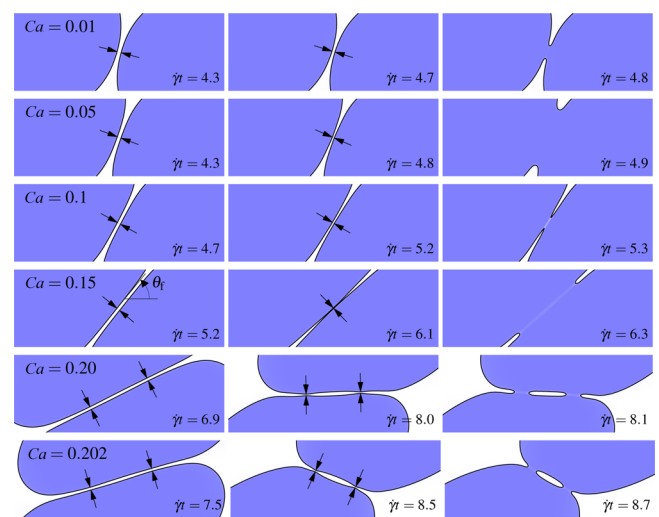


Figure 12. Cross sections through the droplets at the time of slowest film thinning (left), at the last saved time step before coalescence (center), and the first after coalescence (right) for (top to bottom) $Ca = 0.01, 0.05, 0.1, 0.15, 0.2,$ and 0.202 . The time interval between the right pair of images is $\dot{\gamma}\Delta t = 0.133$. Arrows indicate the locations where the films are thinnest.

thinning rate is slowest and at moments before and after coalescence. For $Ca \leq 0.15$, a single point of minimum film thickness exists, while two dimples are present when $Ca \geq 0.2$ and a droplet of the external fluid forms inside the bridge. In the supercritical cases (Figure 11), two dimples are present and the separation between them increases with increasing capillary number. The presence of two dimples is a hydrodynamic feature of a draining film.⁴⁰ As the capillary number decreases to the critical value, the minimum thickness occurs later in the collision process and therefore when the film is inclined further clockwise. At the lowest supercritical capillary number (0.2028), the film slopes downward ($\theta_f = -4.2^\circ < 0$). At subcritical capillary numbers (Figure 12), the minimum thinning rate and coalescence occur later and with further clockwise rotation as the capillary number increases to its critical value. At the low capillary numbers, the film does not rotate significantly between the time of minimum thinning and subsequent coalescence. In contrast, a significant change in inclination can be seen between these two times at $Ca \approx Ca_c$. For $Ca = 0.202$, the minimum thinning rate occurs when the film is inclined upward ($\theta_f = 16^\circ > 0$) while coalescence occurs with a downward-inclined film ($\theta_f = -23^\circ < 0$). Considering the phase portrait of the film thinning process (Figure 7), we hypothesize that as $Ca \rightarrow Ca_c$, the angle at minimum thickness converges to the angle at minimum thinning rate and not the coalescence angle.

Figure 13 summarizes the variation in the film inclination angle as a function of the capillary number at key events in the

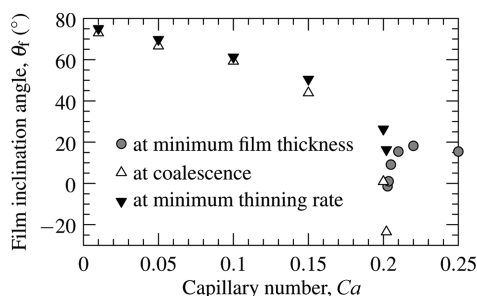


Figure 13. Film inclination angle at several events in the sub- and supercritical collision processes.

sub- and supercritical collision processes, and Figure 14 presents the times of these events. As mentioned previously, the critical events occur later and with a lower film angle as the critical capillary number is approached from above and below. The time between the minimum thinning rate and coalescence increases as $Ca \rightarrow Ca_c$. Since the interaction between colliding

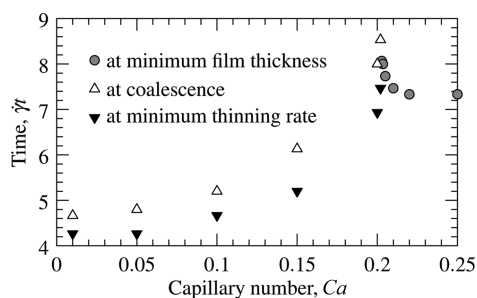


Figure 14. Times of key events in the collision processes at sub- and supercritical capillary numbers.

drops occurs over a finite time interval, maximum times of minimum film thickness, minimum thinning rate, and coalescence must exist. However, the high sensitivity of the film behavior to the capillary number near Ca_c prevents an accurate estimate of these times and the critical angles. Based on the highest subcritical and lowest supercritical simulations, the maximum time for minimum thickness or minimum thinning exceeds $\gamma t = 8.1$ while the maximum coalescence time exceeds 8.5. The corresponding critical angles are $\theta_f < -1.4^\circ$ for minimum film thickness and thinning rate and $\theta_f < -23^\circ$ for coalescence. Considering the small change in spacing between the lines that connect points at the same time in the phase portrait (Figure 7), we estimate an upper bound of $\gamma t \approx 8.4$ on the times of minimum film thickness and thinning rate, from which a lower bound of -17° on the corresponding critical angle is estimated using $\theta_f(\gamma t)$ at the lowest supercritical Ca .

Physical Size of Droplets. To estimate the physical size of the simulated droplets, we compare the critical capillary number of the simulations with experiments at similar conditions. Chen et al.¹⁷ present critical capillary numbers for Newtonian polymer droplets (polydimethylsiloxane in polyisobutylene) with radii between 54 and 158 μm at confinements $2R/H$ up to 0.315. The ratio of the droplet to bulk liquid viscosities was 1.1, and the difference in density was considered negligible. DeBruyn et al.¹⁸ present similar experiments, but their viscosity ratio was 0.1, which we judge to be too low for a meaningful comparison with our current simulations. Guido and Simeone²⁰ did not determine critical capillary numbers for coalescence, but depending on the initial vertical offset, observed sliding and coalescence during extension with a $\sim 100 \mu\text{m}$ radius drop at $Ca = 0.13$ and a viscosity ratio of 0.36. The power law $Ca_c \sim R^{-0.84}$, in which the exponent is independent of the viscosity ratio,⁴¹ fit the confined and unconfined experiments of De Bruyn et al.¹⁸ reasonably, and we use this model to extrapolate experimental Ca_c to smaller drop sizes. Using $Ca_c = 0.0075$ for experiments with $2R = 315 \mu\text{m}$, $2R/H = 0.315$, and $\Delta Y/(2R) = 0.16$,¹⁷ the critical capillary number is $Ca_c = 0.202$ when $R = 3.12 \mu\text{m}$. Use of this power law at high capillary numbers (at which the droplet trajectories deviate from those of rigid spheres) requires caution, since this power law was determined for primarily extensional flow and has not been evaluated experimentally at capillary numbers higher than the 10^{-2} – 10^{-1} range considered by Hu et al.⁴¹ We note also that simulations at an initial offset of 0.6 and 0.86 provided exponents of -1.15 and -1.57 , respectively,³⁰ for critical capillary numbers between 0.02 and 0.2. We consider therefore the effect of a different exponent on the extrapolated physical size: With $Ca_c \sim R^{-1}$, the physical radius is 5.9 μm for the simulated drops; with $Ca_c \sim R^{-0.65}$, it is 1 μm .

A second way to estimate the physical size of the droplets is to consider the ratio of the droplet radius and the critical film thickness. In the simulations, this ratio is 33 based on the extrapolated critical thickness 3.00ζ . An order of magnitude estimate for the critical film thickness for the experimental polymer system is 27 nm.¹⁷ The resulting physical size of the simulated droplets is $R = 0.89 \mu\text{m}$. Extrapolating this size and $Ca_c = 0.202$ to the experimental droplet size with the scaling $Ca_c \sim R^{-0.84}$, we obtain a critical capillary number of 0.0026 for a droplet with $2R = 315 \mu\text{m}$, compared with 0.007–0.008 reported by Chen et al.¹⁷

The two methods for estimating the physical size of the droplets agree to within a factor of 3.5 and indicate a physical radius between 0.9 and 3.1 μm . We consider this agreement to

be reasonable given the uncertainty in determining physical critical film thicknesses, the differences between the experimental and simulated parameters, and uncertainty in the variation of the critical capillary number with drop sizes in the range 1–10 μm where Ca_c is of the order 10^{-1} . This range of droplet sizes is relevant to studies of polymer blends⁴² and emulsions, such as those used in enhanced oil recovery that have mean droplet diameters between 1 and 12 μm .⁴³

Now that an estimate of the physical size of the droplets is available, we may assess whether the interface Péclet number is physically reasonable. For this purpose, we define a modified Péclet number $\hat{P}e$ that is the ratio of the time scale $h_c^2/(MA)$ for phase field diffusion over the critical film thickness and the droplet advection time scale $\dot{\gamma}$:

$$\hat{P}e = \frac{\dot{\gamma}h_c^2}{MA} = Pe \frac{h_c^2}{\zeta R} \quad (7)$$

For the simulations, we have $\hat{P}e = 0.9$, and the two time scales are effectively equal. In the limit $\hat{P}e \gg 1$, interfaces cannot merge because insufficient diffusion occurs over the interaction time of a collision; for $\hat{P}e \ll 1$ diffusion is quick and does not hinder coalescence during the interaction time. To relate the modified Péclet number with the other parameters of the system, we note that

$$\hat{P}e = Re \frac{\nu}{MA} \left(\frac{h_c}{R} \right)^2 \quad (8)$$

The modified Péclet number is thus the product of the Reynolds number, the ratio of the fluid kinematic viscosity and the phase field diffusivity, and the square of the ratio of the critical thickness and droplet radius. We estimate the diffusivity for liquids to be on the order of $10^{-9} \text{ m}^2/\text{s}$, as estimated by Jacqmin.⁴ Using the viscosity of water $\nu = 10^{-6} \text{ m}^2/\text{s}$ and $R/h_c = 33$, we obtain $\hat{P}e = 0.92$. The simulations are therefore at a physically reasonable Péclet number. Since shear rates (and the factors in eq 8) may span many orders of magnitude, for example, 10^{-4} – 10^4 s^{-1} for a typical rheometer, the Péclet numbers for physical systems are expected to span a similarly wide range. Since maximum possible shear rates and micrometer size droplets provide $\hat{P}e$ of order one, $\hat{P}e$ exceeding one are not expected for physical systems unless they have diffusivities much lower than $10^{-9} \text{ m}^2/\text{s}$. Table 1 summarizes the parameters of a sample physical system with the dimensionless parameters of the simulations. The required

Table 1. Parameters of a Sample Physical System with the Same Dimensionless Parameters as the Simulations

parameter	symbol	value
droplet radius	R	1 μm
gap between shear planes	H	5.1 μm
confinement	$2R/H$	0.39
kinematic viscosity (droplet and external)	ν	$10^{-6} \text{ m}^2/\text{s}$
fluid density (droplet and external)	ρ	$10^3 \text{ kg}/\text{m}^3$
shear rate	$\dot{\gamma}$	10^6 s^{-1}
wall speed	u_0	2.6 m/s
wall shear stress	$\rho\nu\dot{\gamma}$	10^3 Pa
Reynolds number	Re	1
interfacial tension	σ	$5 \times 10^{-3} \text{ N}/\text{m}$
capillary number	Ca	0.2

shear rate is below the maximum of a commercially available viscometer (10^7 s^{-1} for the Ultra Shear Viscometer, PCS Instruments, London, U.K.), and the required gap size is larger than the 1.25 μm of this device. The remaining values are typical for liquid systems. The purpose of this comparison is to show that the conditions of the simulations are applicable to physical systems; experiments with droplet collisions at this small size and high shear would need to address challenges such as the generation and observation of the drops. Simulations at lower Re are possible, but would take longer to run since Re would be decreased by reducing the shear rate rather than increasing the fluid viscosity in the LBM we use.

CONCLUSIONS

The interactions between adjacent interfaces during binary droplet collisions in simple shear flow were examined in high resolution phase field simulations with the free-energy lattice Boltzmann method. Large-scale parallel GPU computing was used to simulate droplets with radii spanning $R = 200$ lattice nodes in a $10R \times 5R \times 5R$ domain, of which only one-quarter was computed by exploiting symmetry. The drops had the same density and viscosity as the external fluid, and the Reynolds number of the flow was fixed at one. The critical capillary number for coalescence at a low initial offset between the droplets (20% of the droplet diameters) was determined to within 0.4%. In collisions without coalescence, the difference between the minimum distance and a critical film thickness depends on the difference between the capillary number and the critical capillary number through a simple power law. This relationship was used to estimate a more precise critical capillary number and critical film thickness by fitting the power law to the minimum thicknesses and capillary numbers of several supercritical simulations. At subcritical capillary numbers, an inflection point (and a corresponding minimum thinning rate) exists in the evolution of the minimum film thickness over time. This inflection point occurs before the critical thickness is reached.

The rotating film between the droplets exhibits interesting behavior at near-critical conditions. In this film, the flow relative to rigid rotation at the angular speed of the film reverses from exiting to entering the gap between the drops. The reversal of the (relative) flow coincides with a change in sign of the vorticity in the film. The minimum thickness between the interfaces continues to decrease after the flow reversal due to the phase field mobility. At near-critical capillary numbers, there are two points in the film where it is thinnest. As the critical capillary number is approached from subcritical conditions, the minimum thinning rate and coalescence occur at later times and with further clockwise rotation of the film. When approaching the critical capillary number under supercritical conditions, the minimum film thickness also occurs later and with further film rotation. Due to the high sensitivity of the film behavior to the capillary number (even within 0.5% of the critical value), the details of the film behavior in the critical capillary number limit, such as whether the minimum thinning rate approaches zero or a finite value, remain open questions.

The effective physical size of the simulated droplets could be estimated due to the similarity of the simulated conditions with those of droplet collision experiments in confined shear flow. The use of an empirical scaling for the dependence of the critical capillary number on the size of the droplets provided a 3.1 μm effective physical radius for the simulated droplets. The ratio of the simulated droplet size and the (numerical) critical

film thickness, together with an (order of magnitude) estimate of the critical film thickness for the experimental fluid pair, provided another estimate of the physical size of the simulated droplets: $0.9 \mu\text{m}$. The difference between these estimates is judged reasonable considering the imprecision of the scaling law, critical film thickness, and the differences in properties of the numerical and experimental fluid pair.

The late stages of the interaction between interfaces, specifically at and near the points of minimum distance to the adjacent interface, are determined by the phase field mobility. If it is sufficiently low, this mobility delays the merging of the interfaces. We show that the interface Péclet number Pe of the simulations, which was chosen based on studies of droplet deformation in shear, is reasonable for physical systems. However, a wide range of Péclet numbers is possible, and there is therefore a need to understand the effects of Pe better. Future work could examine how the mobility affects the phase portrait of the film thickness dynamics at near-critical conditions. The effects of the viscosity ratio, initial distance between the drops, and size ratio could also be evaluated. However, further studies of the behavior under one set of conditions and comparison with experimental results are currently more important as they would examine the adequacy of phase field models in describing coalescence physics, thereby revealing the utility of further parameter studies.

Several other avenues are open for future work. Clusters with thousands of GPUs exist, and larger scale computations could be used to further bridge the gap between simulations and experiments. Multiscale modeling of interface behavior would be useful for studies of large-scale flows where films cannot be fully resolved. Studies of relatively small fluid volumes could be used to study drop size distributions and population balance models for their evolution. A question to be addressed by multiscale modeling is whether the simplification that interfaces merge when they reach a critical thickness is reasonable. Considering the small length scales of the simulations, the effects of noncontinuum phenomena are also an area for future work. One aim for future work is to further evaluate the applicability of phase field models to studies of coalescence phenomena and work toward nanoscale direct numerical simulations of interacting interfaces in the spirit of such studies of contact line motion.^{4,44} A second aim is to apply the insights from simulations to flows of many droplets under a wide range of conditions.

■ APPENDIX: CONVERGENCE OF FILM THICKNESS

In this Appendix, we analyze the distance between colliding droplets at the conditions of previous simulations.³⁰ In these simulations, $Re = 1$, $\zeta = 2$, $Ca = 0.1$, $\Delta X/(2R) = 1.26$, $\Delta Y/2R = 0.86$, and $2R/H = 0.39$. The key difference in parameters between the results in this Appendix and the higher-resolution results considered earlier in the paper is the vertical offset $\Delta Y/(2R) = 0.86$. With this vertical offset, the droplets do not coalesce with $Ca = 0.1$ for $R/\zeta \geq 18.75$. We consider two Péclet numbers, 10 and 50, to demonstrate the role of the mobility on the evolution of the minimum film thickness.

Figures 15 and 16 show the minimum distance between the drops as a function time. Of all the cases, only the simulation with $R/\zeta = 18.75$ and $Pe = 10$ is near the critical conditions for coalescence.³⁰ In general, the critical Ca decreases with increasing R/ζ and Pe (increasing mobility M). The difference between the dynamics of h at near-critical conditions is highlighted in Figure 16, in which h/R evolves clearly

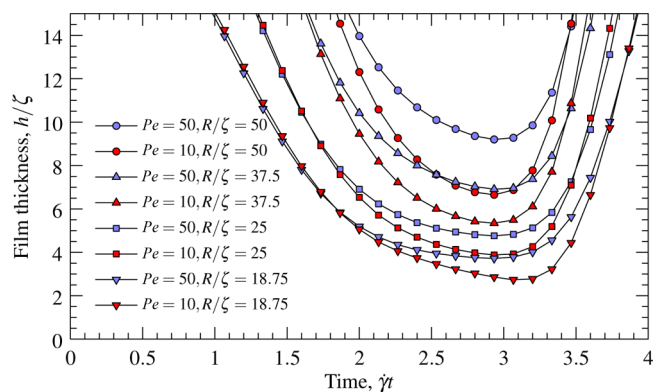


Figure 15. Film thickness (normalized by interface thickness) as a function of time for several resolutions at noncoalescing conditions ($Ca = 0.1$, $\Delta Y/(2R) = 0.86$) and two Péclet numbers. For all cases, $\zeta = 2$.

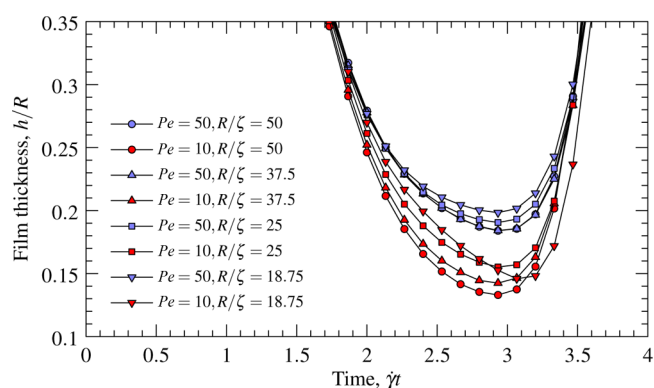


Figure 16. Film thickness normalized by the droplet radius R at the same conditions as in Figure 15

differently from the other cases. In this near-critical case, h has a longer period of thinning and a later minimum. In the other cases, convergence toward different limits is seen for the two Péclet numbers. With the higher mobility (lower Pe), the minimum thickness of the film is lower, consistent with the expectation that the late stages of thinning are determined by the mobility rather than fluid flow in the film. In Figure 15, we see that the curves for the smallest radius cross at $\gamma t = 1.7$ and $h/\zeta = 6$. Until this point, one may consider the interfaces to be noninteracting because the thickness of the film is independent of the mobility.

■ AUTHOR INFORMATION

Corresponding Author

*E-mail: shardt@ualberta.ca.

Notes

The authors declare no competing financial interest.

■ ACKNOWLEDGMENTS

This research has been enabled by the use of computing resources provided by WestGrid, the Shared Hierarchical Academic Research Computing Network (SHARCNET: www.sharcnet.ca), and Compute/Calcul Canada. O.S. is supported by an Alexander Graham Bell Canada Graduate Scholarship from NSERC.

■ REFERENCES

- (1) van der Sman, R.; van der Graaf, S. Emulsion droplet deformation and breakup with lattice Boltzmann model. *Comput. Phys. Commun.* **2008**, *178*, 492–504.
- (2) Komrakova, A.; Shardt, O.; Eskin, D.; Derksen, J. Lattice Boltzmann simulations of drop deformation and breakup in shear flow. *Int. J. Multiphase Flow* **2014**, *59*, 24–43.
- (3) van der Graaf, S.; Nisisako, T.; Schroën, C.; van der Sman, R.; Boom, R. Lattice Boltzmann simulations of droplet formation in a T-shaped microchannel. *Langmuir* **2006**, *22*, 4144–4152.
- (4) Jacqmin, D. Contact-line dynamics of a diffuse fluid interface. *J. Fluid Mech.* **2000**, *402*, 57–88.
- (5) Qian, T.; Wang, X.-P.; Sheng, P. Molecular scale contact line hydrodynamics of immiscible flows. *Phys. Rev. E* **2003**, *68*, 016306.
- (6) Briant, A.; Yeomans, J. Lattice Boltzmann simulations of contact line motion. II. Binary fluids. *Phys. Rev. E* **2004**, *69*, 031603.
- (7) Yue, P.; Feng, J. Can diffuse-interface models quantitatively describe moving contact lines? *Eur. Phys. J.: Spec. Top.* **2011**, *197*, 37–46.
- (8) Cahn, J.; Hilliard, J. Free energy of a nonuniform system. I. Interfacial free energy. *J. Chem. Phys.* **1958**, *28*, 258–267.
- (9) Qian, T.; Wang, X.-P.; Sheng, P. A variational approach to moving contact line hydrodynamics. *J. Fluid Mech.* **2006**, *564*, 333–360.
- (10) Jia, X.; McLaughlin, J. B.; Kontomaris, K. Lattice Boltzmann simulations of flows with fluid–fluid interfaces. *Asia-Pac. J. Chem. Eng.* **2008**, *3*, 124–143.
- (11) Farhat, H.; Lee, J. Suppressing the coalescence in the multi-component lattice Boltzmann method. *Microfluid. Nanofluid.* **2010**, *11*, 137–143.
- (12) Spencer, T.; Halliday, I.; Care, C. A local lattice Boltzmann method for multiple immiscible fluids and dense suspensions of drops. *Philos. Trans. R. Soc. London, A* **2011**, *369*, 2255–2263.
- (13) Bremond, N.; Thiam, A.; Bibette, J. Decompressing emulsion droplets favors coalescence. *Phys. Rev. Lett.* **2008**, *100*, 024501.
- (14) Zawadzki, I.; Antonio, M. Equilibrium raindrop size distributions in tropical rain. *J. Atmos. Sci.* **1988**, *45*, 3452–3459.
- (15) Tsouris, C.; Tavlarides, L. Breakage and coalescence models for drops in turbulent dispersions. *AIChE J.* **1994**, *40*, 395–406.
- (16) Perlekar, P.; Biferale, L.; Sbragaglia, M.; Srivastava, S.; Toschi, F. Droplet size distribution in homogeneous isotropic turbulence. *Phys. Fluids* **2012**, *24*, 065101.
- (17) Chen, D.; Cardinaels, R.; Moldenaers, P. Effect of confinement on droplet coalescence in shear flow. *Langmuir* **2009**, *25*, 12885–12893.
- (18) De Bruyn, P.; Cardinaels, R.; Moldenaers, P. The effect of geometrical confinement on coalescence efficiency of droplet pairs in shear flow. *J. Colloid Interface Sci.* **2013**, *409*, 183–192.
- (19) Loewenberg, M.; Hinch, E. Collision of two deformable drops in shear flow. *J. Fluid Mech.* **1997**, *338*, 299–315.
- (20) Guido, S.; Simeone, M. Binary collision of drops in simple shear flow by computer-assisted video optical microscopy. *J. Fluid Mech.* **1998**, *357*, 1–20.
- (21) Cristini, V.; Bławdziewicz, J.; Loewenberg, M. An adaptive mesh algorithm for evolving surfaces: Simulations of drop breakup and coalescence. *J. Comput. Phys.* **2001**, *168*, 445–463.
- (22) Bartok, W.; Mason, S. Particle motions in sheared suspensions. VIII. Singlets and doublets of fluid spheres. *J. Colloid Sci.* **1959**, *14*, 13–26.
- (23) Allan, R.; Mason, S. Particle motions in sheared suspensions. IV. Coalescence of liquid drops in electric and shear fields. *J. Colloid Sci.* **1962**, *17*, 383–408.
- (24) Yang, H.; Park, C.; Hu, Y.; Leal, L. The coalescence of two equal-sized drops in a two-dimensional linear flow. *Phys. Fluids* **2001**, *13*, 1087–1106.
- (25) Yoon, Y.; Borrell, M.; Park, C.; Leal, L. Viscosity ratio effects on the coalescence of two equal-sized drops in a two-dimensional linear flow. *J. Fluid Mech.* **2005**, *525*, 355–379.
- (26) Mousa, H.; Agterof, W.; Mellema, J. Experimental investigation of the orthokinetic coalescence efficiency of droplets in simple shear flow. *J. Colloid Interface Sci.* **2001**, *240*, 340–348.
- (27) Olapade, P.; Singh, R.; Sarkar, K. Pairwise interactions between deformable drops in free shear at finite inertia. *Phys. Fluids* **2009**, *21*, 063302.
- (28) Singh, R.; Sarkar, K. Effects of viscosity ratio and three dimensional positioning on hydrodynamic interactions between two viscous drops in a shear flow at finite inertia. *Phys. Fluids* **2009**, *21*, 103303.
- (29) Sarkar, K.; Singh, R. Spatial ordering due to hydrodynamic interaction between a pair of colliding drops in a confined shear. *Phys. Fluids* **2013**, *25*, 051702.
- (30) Shardt, O.; Derksen, J.; Mitra, S. Simulations of droplet coalescence in simple shear flow. *Langmuir* **2013**, *29*, 6201–6212.
- (31) Aidun, C.; Clausen, J. Lattice-Boltzmann method for complex flows. *Annu. Rev. Fluid Mech.* **2010**, *42*, 439–472.
- (32) Bhatnagar, P.; Gross, E.; Krook, M. A model for collision processes in gases. I: Small amplitude processes in charged and neutral one-component system. *Phys. Rev.* **1954**, *94*, 511–525.
- (33) Ladd, A. Numerical simulations of particulate suspensions via a discretized Boltzmann equation. Part 1. Theoretical foundation. *J. Fluid Mech.* **1994**, *271*, 285–309.
- (34) Tjahjadi, M.; Stone, H.; Ottino, J. Satellite and subsatellite formation in capillary breakup. *J. Fluid Mech.* **1992**, *243*, 297–317.
- (35) Khismatullin, D.; Renardy, Y.; Cristini, V. Inertia-induced breakup of highly viscous drops subjected to simple shear. *Phys. Fluids* **2003**, *15*, 1351–1354.
- (36) Hammerlindl, A.; Bowman, J.; Prince, T. *Asymptote: The Vector Graphics Language*; <http://asymptote.sourceforge.net/>, 2004–2014.
- (37) Tryggvason, G.; Bunner, B.; Esmaeeli, A.; Juric, D.; Al-Rawahi, N.; Tauber, W.; Han, J.; Nas, S.; Jan, Y.-J. A front-tracking method for the computations of multiphase flow. *J. Comput. Phys.* **2001**, *169*, 708–759.
- (38) Quan, S.; Lou, J.; Schmidt, D. Modeling merging and breakup in the moving mesh interface tracking method for multiphase flow simulations. *J. Comput. Phys.* **2009**, *228*, 2660–2675.
- (39) Kuzmin, A.; Januszewski, M.; Eskin, D.; Mostowfi, F.; Derksen, J. Simulations of gravity-driven flow of binary liquid in microchannels. *Chem. Eng. J.* **2011**, *171*, 646–654.
- (40) Chesters, A. The modelling of coalescence processes in fluid-liquid dispersions: A review of current understanding. *Chem. Eng. Res. Des.* **1991**, *69*, 259–270.
- (41) Hu, Y.; Pine, D.; Leal, L. Drop deformation, breakup, and coalescence with compatibilizer. *Phys. Fluids* **2000**, *12*, 484–489.
- (42) Sundararaj, U.; Macosko, C. Drop breakup and coalescence in polymer blends: The effects of concentration and compatibilization. *Macromolecules* **1995**, *28*, 2647–2657.
- (43) McAuliffe, C. D. Oil-in-water emulsions and their flow properties in porous media. *J. Pet. Technol.* **1973**, *24*, 727–733.
- (44) Jacqmin, D. Calculation of two-phase Navier-Stokes flows using phase-field modeling. *J. Comput. Phys.* **1999**, *155*, 96–127.